3D surface-based registration of ultrasound and histology in prostate cancer imaging

Computerized Medical Imaging and Graphics 47 (2016) 29–39

Contents lists available at ScienceDirect

Computerized Medical Imaging and Graphics

journal homepage: www.elsevier.com/locate/compmedimag

3D surface-based registration of ultrasound and histology in prostate cancer imaging

Stefan G. Schalk[a,*], Arnoud Postema[b], Tamerlan A. Saidov[a], Libertario Demi[a], Martijn Smeenge[b], Jean J.M.C.H. de la Rosette[b], Hessel Wijkstra[a,b], Massimo Mischi[a]

[a] Department of Electrical Engineering, Eindhoven University of Technology, Postbus 513, 5600 MB Eindhoven, The Netherlands
[b] Department of Urology, AMC University Hospital, Meibergdreef 9, 1105 AZ Amsterdam, The Netherlands

ARTICLE INFO

Article history:
Received 25 March 2015
Received in revised form 13 July 2015
Accepted 3 November 2015

Keywords:
3D registration
Prostate
Ultrasound
Histology
Deformable model
Elastic registration

ABSTRACT

Several transrectal ultrasound (TRUS)-based techniques aiming at accurate localization of prostate cancer are emerging to improve diagnostics or to assist with focal therapy. However, precise validation prior to introduction into clinical practice is required. Histopathology after radical prostatectomy provides an excellent ground truth, but needs accurate registration with imaging. In this work, a 3D, surface-based, elastic registration method was developed to fuse TRUS images with histopathologic results. To maximize the applicability in clinical practice, no auxiliary sensors or dedicated hardware were used for the registration. The mean registration errors, measured *in vitro* and *in vivo*, were 1.5 ± 0.2 and 2.1 ± 0.5 mm, respectively.

1. Introduction

Prostate cancer (PCa) is the type of cancer with the highest incidence and second highest mortality among males in the United States [1]. Despite the statistics of this cancer type, the main diagnostic technique, systematic biopsy, has major drawbacks. Firstly, being invasive, it can cause infections and hematuria [2]. Secondly, tumors can be missed by the biopsy needle [3], resulting in poor sensitivity of this diagnostic tool. Thirdly, tumors can be undergraded when the more aggressive region of a tumor is missed [4], leading to undertreatment. Moreover, because of the lack of reliable localization methods, PCa is often overtreated out of precautionary considerations [5,6], increasing risk of urinary incontinence and impotence [5].

To overcome these limitations, several methods aiming at non-invasive PCa localization are currently under development. Determining the exact location of PCa would decrease the number of biopsies and the chance of missing cancerous tissue by use of targeted biopsies [7]. In addition, it can enable imaging-targeted focal therapy as a treatment option [7,8]. Currently, most studies involving PCa localization are based on magnetic resonance (MR) imaging [9–11]. However, studies using transrectal ultrasound (TRUS)-based methods – such as computer-assisted TRUS [12,13], (shear-wave) elastography [14–17], and dynamic contrast-enhanced ultrasound [18,19] – also show promising results. TRUS has the advantages over MR of being less expensive, widely used for targeting biopsies, and directly applicable by urologists.

Because of the lack of a medical imaging modality revealing the exact location of cancerous tissue in the prostate, histopathologic analysis after radical prostatectomy (RP, excision of the prostate) is frequently used as a gold standard for validation of new imaging techniques [9,20–24]. Usually, the excised prostate is sectioned into 3- to 4-mm-thick slices, after which the separate slices are compared with the images used for PCa localization [25]. However, due to the different orientation of the imaging planes and the histology slices, one image could span multiple histology planes. Deformation of the prostate caused by pressure from transrectal probe or due to surgery and preparation for histopathologic analysis can further complicate accurate validation. Moreover, the histology slice corresponding to the image has to be manually selected, endangering the objectivity of the validation. A 3-dimensional (3D) registration method could assist in making an objective and accurate comparison between the PCa imaging technique and the gold standard.

Extensive work has already been done on *in vivo* MR-pathology mapping of the prostate, which is a challenging task, because of the deformation due to surgery and to preparation of the tissue for

* Corresponding author. Tel.: +31 402473918.
E-mail address: s.g.schalk@tue.nl (S.G. Schalk).

http://dx.doi.org/10.1016/j.compmedimag.2015.11.001
0895-6111/

histologic analysis. In some methods [26,27], the histology slices corresponding to the MR slices are manually selected after which 2D registration is applied. In another approach [28], the algorithm tries to find the corresponding slices automatically prior to their registration. However, in TRUS, the histology slices are typically not aligned with the imaging planes.

In other studies, fiducial markers [29,30], manually outlined natural landmarks [29], and a 3D-printed mold of the prostate [21,31,32] were used to assist with the registration. Some researchers [33,30] used *ex vivo* MR images to break down the registration in smaller steps. Although improving the registration accuracy, the extra steps could conflict with the clinical workflow in most hospitals.

In contrast to MR-histology registration, only few research groups have made attempts to register prostate ultrasound (US) imaging withhistology. Taylor et al. [34] implemented a semi-automatic 6-degrees-of-freedom (DOF) rigid body registration algorithm to match the surface of an excised prostate imaged by US with the surface of the same prostate after fixation for histology. The registration was used for validation of a cancer detection method using sonoelastography. However, the registration accuracy was estimated completely *ex vivo*. In [35], the authors described a method for elastic registration of a prostate recorded by *in vivo* TRUS imaging and histology. An ellipsoid fit and the position of the urethra were used to align the images by affine transformation, but no information on the registration error was given. Recently, a technique was proposed in [36] to jointly align histology slices to intra-operative 3D US by affine transformations using particle filtering. Again, except for the area overlap between the registered histology slices and the corresponding cross-sections in US, no information was provided on the accuracy of the method.

This paper describes a new method to elastically register TRUS and histology in 3D for validation or training of TRUS-based PCa imaging techniques. TRUS-histology registration is a challenging task for reasons concerning both TRUS and histology. The main challenges concerning TRUS are summarized below:

- the orientations of the TRUS imaging planes are unknown without use of additional sensors;
- usually, no reliable natural landmarks are visible in both TRUS imaging and histology to assist with the registration;
- introduction of the transrectal probe causes a local posterior deformation,

whereas these are the biggest obstacles concerning histology:

- for histological analysis, the prostate is cut into 3- to 4-mm-thick slices, providing poor resolution in that direction;
- after excision, the prostate is relieved from pressure caused by surrounding organs and tissue, resulting in a deformation;
- fixation of the prostate after RP causes a volume decrease [37].

To avoid the need of landmarks or a high level of detail, which are lacking in B-mode TRUS, the method presented here is surface-based, requiring prostate shape information only. Both the affine and local deformations of the prostate as a result of the probe pressure and deformation after excision are taken into account. Apart from acquiring the prostate shapes, no manual intervention is required during the registration process. Moreover, being independent of the underlying imaging modality, application of the method in validation of PCa imaging techniques using other modalities (*e.g.*, MR or CT) could be a feasible option.

In other work related to surface-based, elastic registration of prostates, Crouch et al. [38] estimated boundary displacements by minimizing deformation energy. After that, a uniform, nearly-incompressible material with linear elasticity was assumed to estimate internal deformation. Lee et al. [39] developed a technique for a joint estimation of elasticity and deformation of organs and tested it on ten prostates. Parameters describing the mechanical properties and forces acting on the boundary of the prostate were optimized through minimization of the distance between the prostate surfaces to register.

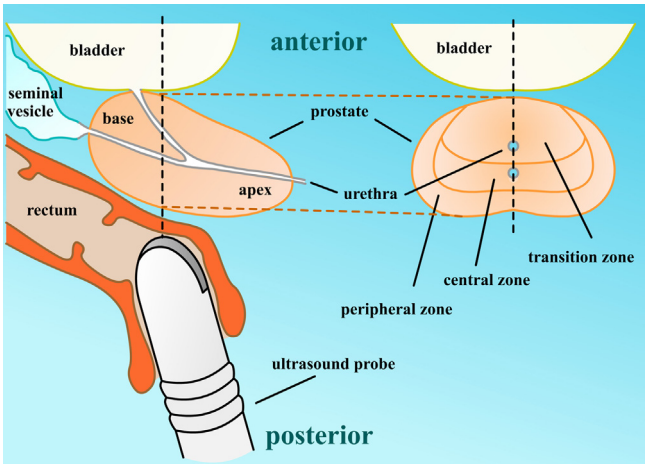

Fig. 1. Schematic illustration of the prostate with surrounding structures (left) and a transversal cut showing the zonal anatomy (right).

The method presented in this paper does not rely on the underlying patient-specific mechanical properties, which may be difficult to determine during an examination and may change during the fixation process as part of the preparation for histopathologic analysis. Moreover, values for Young's modulus of prostate tissue found in literature vary in order from 10 to 100 kPa [40–44]; additionally, varying values of stiffness among different prostate zones were reported [40]. For these reasons, internal deformation is estimated based on shape difference only. In this way, the method can be applied using data obtained during a routine prostate examination by TRUS imaging without the use of specialized equipment or training.

Because of the 2D nature of TRUS imaging as commonly used in clinical practice, an additional step consisted of the construction of a 3D surface model based on the prostate contours in multiple 2D TRUS images. The reconstruction of 3D surfaces from 2D images can be performed in various ways [45–48] and is not the focus of this paper. However, for completeness, the method we designed for our study is also described.

In an *in vitro* experiment, the registration algorithm's accuracy was assessed in 2 gelatin phantoms with fiducial markers. Additionally, in an *in vivo* experiment, we used the border between the peripheral and central zone (BPZ) to estimate the method's target registration error (TRE) in 7 patients. To the authors' knowledge, no quantitative *in vivo* validation has yet been reported for 3D registration between TRUS and histology.

2. Material and methods

2.1. Prostate anatomy

The prostate is part of the male reproductive system and is located between the bladder and the rectum. A schematic overview of the prostate anatomy is given in Fig. 1, in which the position of the TRUS imaging probe has also been drawn. This illustration indicates the locations of the base and apex, and posterior and anterior side, which are frequently mentioned throughout this paper. In addition, a schematic overview of the zonal anatomy is shown in a transversal plane.

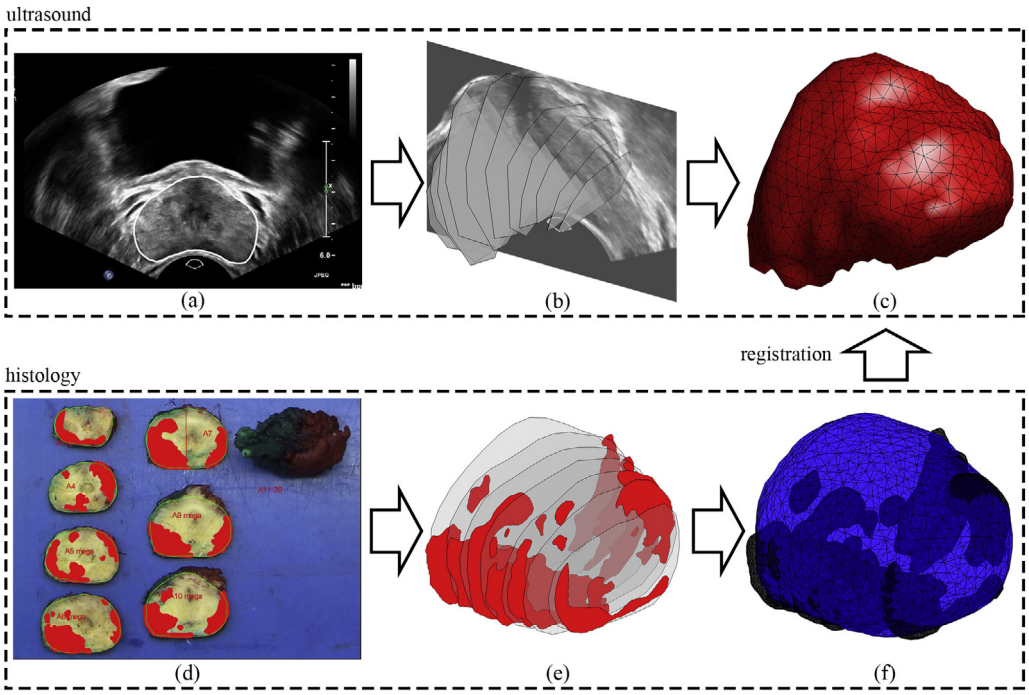

Fig. 2. Schematic overview of the construction and registration of the prostate shape models obtained from ultrasound and histology. (a) One frame of the transversal sweep video with outlined prostate contour. (b) Longitudinal image with prostate contours from the transversal video. (c) Final surface mesh of the prostate obtained from TRUS imaging (after remeshing). (d) Macro-photo of prostate slices prepared for histology with cancerous tissue marked in red. (e) Positioning of the prostate contours and tumors in 3D. (f) Resulting surface mesh of the prostate obtained from histology (after remeshing). (For interpretation of the references to color in this figure legend, the reader is referred to the web version of the article.)

2.2. Surface reconstruction

2.2.1. TRUS

To perform 3D registration of TRUS and histology shapes, 3D triangulated meshes of the prostate shapes in both modalities were constructed. First, a TRUS video of the prostate, from now on referred to as "transversal sweep video", was recorded *in vivo* using a Philips iU22 US scanner (Philips Healthcare, Bothell, WA) with an end-fire probe in B-mode by inserting the probe rectally until it reached the prostate and steadily rotating it to move its tip from base to apex. Additionally, a longitudinal image in the mid-sagittal plane, which is perpendicular to the images in the sweep video, was recorded. The prostate boundaries were manually outlined by an expert in approximately 30 of the frames in the transversal video, as shown for one frame in Fig. 2(a), which would be used to construct the 3D model.

From the longitudinal image, the angles θ_{base} and θ_{apex} of the first and last transversal frames with the probe center line were determined (see Fig. 3). The center of rotation was initially chosen as indicated in Fig. 3. To estimate the angles of the other frames, linear interpolation was applied; *i.e.*, a constant angular velocity of the probe was assumed. The manually drawn contours were then positioned in a 3D Euclidian space. After visual comparison of the positioned contours with the longitudinal image (Fig. 2(b)), the center of rotation could be moved vertically, and θ_{base} and θ_{apex} could be adjusted.

A triangulated mesh was created by connecting vertices on neighboring contours (Fig. 2(c)). Finally, thin caps were added to the base and apex to prevent sharp edges at the first and last contours.

2.2.2. Histology

Because histopathologic analysis of the prostate after excision was used as a gold standard, patients were only included in this study if they were diagnosed with PCa and underwent RP. After RP, the prostate was submerged in a formalin solution for approximately 24 h, possibly producing the side-effect of prostate shrinkage [37]. Then, the distal caps of the prostate were removed by a transversal cut at approximately 4 mm from the apex and base. The remaining prostate was then transversally sectioned in slices with a thickness of 4 mm and prepared for microscopic examination.

A macro-photo of all slices was taken (example shown in Fig. 2(d)), in which the prostate contours were drawn. Additionally, any tumors found by histopathology were added to the photo in red. By manually aligning the slices with the contours and placing them behind each other with 4 mm distance in between (Fig. 2(e)), a 3D prostate shape (including tumors) was reconstructed. A triangulated mesh was obtained by linear connection between vertices in adjacent slices (Fig. 2(f)). Finally, the distal caps of the prostate,

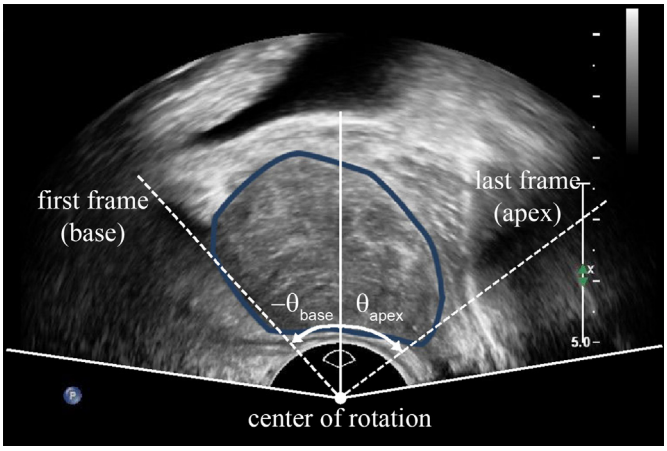

Fig. 3. Illustration of the angles θ_{base} and θ_{apex} of the first and last frame of the transversal sweep video in a longitudinal image. The initial estimation of the center of rotation of the TRUS probe has also been indicated.

which had been cut off before, were measured and added to the base and apex of the model to close it.

2.3. Registration algorithm

An image registration process can in general be described as the search for the spatial mapping $\mathcal{S}(\mathbf{x})$ that best aligns a source image $\mathbf{I}_S$ with a reference image $\mathbf{I}_R$ by moving the image coordinates $\mathbf{x}$:

$$\hat{\mathbf{I}}_R(\mathbf{x}) = \mathbf{I}_S(\mathcal{S}(\mathbf{x})). \tag{1}$$

The registered image $\hat{\mathbf{I}}_R$ is an estimation of $\mathbf{I}_R$. In our case, the source image was the histology prostate model and the reference image was the TRUS prostate model.

Our registration algorithm consisted of three steps:

1. an affine, global registration,
2. an elastic surface registration,
3. an internal registration, which interpolates the deformation of the surface in step 2 to the inner volume.

In step 1, we accounted for the global difference in position, orientation and size by an affine mapping, whereas the local deformations, as a result of probe pressure and radical prostatectomy, were compensated for in steps 2 and 3 by an elastic mapping. The total mapping function was the concatenation of the affine and elastic mapping, $\mathcal{T}_{aff}$ and $\mathcal{T}_{el}$, respectively:

$$\mathcal{T}(\mathbf{x}) = \mathcal{T}_{el}(\mathcal{T}_{aff}(\mathbf{x})). \tag{2}$$

2.3.1. Step 1: affine registration

The affine registration globally aligned the prostate model and served as initialization for the subsequent steps, which made it a very crucial step. We tested two different approaches: an iterative closest point (ICP) algorithm [49] and a stepwise method in which translation, rotation and scaling were implemented as sequential steps. As an initialization to both approaches, the midpoints – defined as the means $\bar{\mathbf{x}}_R$ and $\bar{\mathbf{x}}_S$ of the surface vertex coordinates of the reference and source models, respectively – were aligned by translating the source model.

The ICP algorithm [49] iteratively finds corresponding vertices on the prostate models and minimizes the root-mean-square (RMS) distance between those vertices by transforming the source model. In [49], where only rigid body transformations (translation + rotation) were considered, a direct solution [50] for the minimum RMS was applied.

Besides a rigid body transformation, we also tested two non-rigid transformations: a rigid body transformation followed by an isotropic scaling (IS) and a rigid body transformation followed by an anisotropic scaling (AS). Scaling was implemented to compensate for volume difference and global shape changes, mainly due to operations on the prostate after excision. Moreover, it provided a close match of the prostate surfaces as initialization for the elastic surface registration in the next step. To find the minimum RMS for the non-rigid transformations, we used a Levenberg–Marquardt optimizer [51,52].

In the stepwise approach to affine registration, first, the three main axes of both shapes were estimated by principal component analysis (PCA) of the surface vertex coordinates, as elaborated in [53]. Numerically, the principal components were computed as the eigenvectors of the symmetric $P \times P$ covariance matrix $\mathbf{C}$ of the P observed variables, which in our case was defined as:

$$\mathbf{C} = \begin{bmatrix} \mathrm{cov}(\mathbf{x}_O, \mathbf{x}_O) & \mathrm{cov}(\mathbf{x}_O, \mathbf{y}_O) & \mathrm{cov}(\mathbf{x}_O, \mathbf{z}_O) \\ \mathrm{cov}(\mathbf{y}_O, \mathbf{x}_O) & \mathrm{cov}(\mathbf{y}_O, \mathbf{y}_O) & \mathrm{cov}(\mathbf{y}_O, \mathbf{z}_O) \\ \mathrm{cov}(\mathbf{z}_O, \mathbf{x}_O) & \mathrm{cov}(\mathbf{z}_O, \mathbf{y}_O) & \mathrm{cov}(\mathbf{z}_O, \mathbf{z}_O) \end{bmatrix}, \tag{3}$$

with $\mathrm{cov}(\bullet, \bullet)$ represented the covariance operator and $\mathbf{x}_O$, $\mathbf{y}_O$, and $\mathbf{z}_O$ the observation vectors containing the x-, y-, z-components of the model vertices $\mathbf{x}$.

Let $\mathbf{V}_R$ and $\mathbf{V}_S$ be the 3×3 orthonormal matrix containing by column the eigenvectors (sorted by eigenvalue) of the covariance matrices for the reference and source models, respectively. These matrices represent the orientations of the models, but are not uniquely defined, because of the possible inverse direction of the eigenvectors. We could, however, assume a reasonable initial alignment, because both models were similarly obtained by stacking contours from apex to base. For this reason, we swapped the columns in $\mathbf{V}_R$ and $\mathbf{V}_S$ such that the largest absolute values in each column were on the diagonal, and multiplied any column by -1 for which the entry on the diagonal was negative. By doing this, we limited the rotation angle to 90°.

Having found the orientations $\mathbf{V}_R$ and $\mathbf{V}_S$, a rotation matrix $\mathbf{R}$, which transforms $\mathbf{V}_S$ into $\mathbf{V}_R$ was obtained by:

$$\mathbf{R} = \mathbf{V}_R \mathbf{V}_S^{-1} = \mathbf{V}_R \mathbf{V}_S^T. \tag{4}$$

The individual coordinates $\mathbf{x}_S$ of the source surface model are now registered by combining the translation and rotation:

$$\mathbf{x}_S^{(r)} = \mathbf{R}(\mathbf{x}_S - \bar{\mathbf{x}}_S) + \bar{\mathbf{x}}_R. \tag{5}$$

Scaling (IS or AS) was implemented as the next step in the stepwise method. Mathematically, the source surface coordinates were pre-multiplied by a scaling matrix $\mathbf{S}$:

$$\mathbf{S} = \begin{bmatrix} s_a & 0 & 0 \\ 0 & s_b & 0 \\ 0 & 0 & s_c \end{bmatrix}. \tag{6}$$

For IS ($s_a = s_b = s_c$), the scaling factor was chosen such that the volumes of the models were equal after scaling. In the AS approach, the scaling factors s_a, s_b, and s_c were estimated by projecting the surface nodes of each model onto each principal axis $\mathbf{a}$, $\mathbf{b}$, $\mathbf{c}$ of that model and calculating the ratio between the root mean squared distances $d_{\mathbf{a}}$, $d_{\mathbf{b}}$, and $d_{\mathbf{c}}$ between the coordinates projected on these axes to the model center:

$$s_a = \frac{d_{\mathbf{a}_R}}{d_{\mathbf{a}_S}}, \quad s_b = \frac{d_{\mathbf{b}_R}}{d_{\mathbf{b}_S}}, \quad s_c = \frac{d_{\mathbf{c}_R}}{d_{\mathbf{c}_S}}. \tag{7}$$

The subscripts R and S in (7) refer to the reference and source models, respectively.

The complete affine transformation for the stepwise approach was found by combining all previous steps:

$$\mathcal{T}_{aff}(\mathbf{x}) = \mathbf{V}_R \mathbf{S} \mathbf{V}_S^T (\mathbf{x} - \bar{\mathbf{x}}_S) + \bar{\mathbf{x}}_R. \tag{8}$$

2.3.2. Step 2: elastic surface registration

For elastic registration of the surfaces, we used a parametric active contour model, based on the algorithms described in [54–56], commonly used for segmentation or motion tracking in medical images (see *e.g.* [57–59]). One advantage of this technique is its capability to project nodes from the source model onto the reference model while maintaining a natural spreading of the nodes. Another advantage is the intrinsic smoothing of the surface, which makes the registration less susceptible to irregularities in the prostate models. The main steps of this algorithm are described below; for a detailed description, the reader is referred to [56].

Registration is performed by minimizing an energy functional

$$E = \int_{\Omega} (E_{\mathrm{int}}(\mathbf{s}) + E_{ext}(\mathbf{s}))dA \tag{9}$$

by applying a transformation $\mathbf{s} : \Omega \subset \mathbb{R}^2 \rightarrow \mathbb{R}^3$ to a surface Ω [56]. E_{int} represents the internal energy, defined by the surface material properties, whereas the external energy E_{ext} is defined by the

Table 1
Parameter values in the active contour algorithm.

Symbol	Description	Value
$\Delta p_{\min}$	Stopping criterion (mm)	0.03
α	Resists stretching	0.01
β	Resists bending	0.1
γ	Time step	0.5
σ	Reference image blurring coefficient (mm)	1.67
κ	External force factor	3
λ	Normal force factor	0.2

reference image $\mathbf{I}_R$. In our case, $\mathbf{I}_R$ was a binary voxel image of the TRUS reference volume with a resolution of 1/3 mm per voxel. The internal and external energy are calculated by [56]

$$E_{\text{int}}(\mathbf{s}) = \sum_{i=1}^{3} \alpha \|\nabla \mathbf{s}_i\|_2^2 + \beta(\|\nabla^2 \mathbf{s}_i\|_2^2 - 2|H(\mathbf{s}_i)|), \tag{10}$$

$$E_{ext}(\mathbf{s}) = -\kappa \|(\nabla[G_\sigma * \mathbf{I}_R])(\mathbf{s})\|_2, \tag{11}$$

in which $\mathbf{s}_i$ denotes the ith spatial component of $\mathbf{s}$, $H(\cdot)$ represents the Hessian matrix, G_σ is a 3D Gaussian kernel with standard deviation σ, and κ is the external force factor, determining the weight of the external force [56]. The parameters α and β control the surface properties and accomplish a membrane-like or a thin-plate-like behavior, respectively.

A local minimum of (9) can be found by the iterative solution

$$\mathbf{p}_{i+1} = \mathbf{p}_i + \gamma(\alpha U(\mathbf{p}_i) - \beta U^2(\mathbf{p}_i) - \lambda(\mathbf{N} \cdot \nabla E_{ext}(\mathbf{p}_i))\mathbf{N} - (1-\lambda)\nabla E_{ext}(\mathbf{p}_i)), \tag{12}$$

in which $\mathbf{p}_i$ contains the coordinates of a surface node in the ith iteration and γ is the step size of each iteration. The operator $U(\cdot)$ represents the Umbrella function as defined in [56].

Forces tangent to the mesh surface can cause self-intersection within the mesh. To prevent the surface mesh from self-intersecting, the external force vector, ∇E_{ext}, was replaced in (12) by a weighted sum of the external force vector and the vertex normal vector $\mathbf{N}$ as suggested in [56]. The parameter $\lambda \in [0, 1]$ determines the influence of the image force relative to the surface normal.

The algorithm stops when the maximum node displacement per step size falls below Δp_{min}. After the algorithm had stopped, we defined the elastic mapping $\mathcal{T}_{el}(\mathrm{p_0})$ of each node position of the initial surface mesh to be the displacement $\mathbf{p}_{end} - \mathbf{p}_0$ of that vertex at the end of the algorithm.

The parameter values were empirically optimized based on the registration of the prostate models of 5 test patients. First, the standard deviation of the Gaussian filter σ was set to a value such that the blurred reference image entirely covered the source model. Next, a value for λ was chosen sufficiently large to prevent self-intersection, but as low as possible to keep disturbance of the external energy field to a minimum. The parameters α, β, κ, and γ were heuristically determined to achieve a fast convergence, while keeping the registration smooth and stable. All parameter values are summarized in Table 1.

2.3.3. Step 3: internal registration

To estimate the elastic transformation $\mathcal{T}_{el}$ for the interior of the prostate, the surface vertex displacements found by the elastic surface registration were interpolated. We tested two different ways of interpolating the vertex displacements.

The first method was a finite element (FE) approach assuming a linearly-elastic, nearly-incompressible material (Young's modulus 25 kP, Poisson's ratio 0.495), similar to the material properties used in [60,38]. To this end, a tetrahedral mesh was generated using TetGen 1.4.3 [61] with the quality measure q set to its maximum value (*i.e.*, 18).

In the second method, we used a natural neighbor (NN) interpolation method [62] to interpolate the surface displacements in each dimension separately. This method is based on the Voronoi diagram of the coordinates at which the displacements to be interpolated are known. To obtain the displacement at a new coordinate, a new Voronoi diagram is constructed around this coordinate. The interpolated value is then calculated as the weighted sum of the displacements at the coordinates whose old Voronoi cells overlap the Voronoi cell of the new coordinate to obtain a smooth interpolation. This technique has the advantage over FE-based methods that no internal mesh has to be generated and no prior knowledge about the mechanical properties of the underlying material is required or used.

To find the complete deformation field of the prostate, the affine and elastic deformations were concatenated by applying (2). Tumors found by histology could now be reconstructed in the analyzed TRUS plane by mapping all points of the tumor model to their corresponding positions in the TRUS model according to (1).

2.3.4. Implementation

The registration algorithm described in this section was implemented in MATLAB 8.4.0.150421 (The MathWorks, Natick, MA) on a PC using an Intel® Core i5-2500 processor running at 3.3 GHz (Intel, Santa Clara, CA) with 16 GB RAM. Our implementation of the ICP algorithm in MATLAB was based on functions written by Kroon [63] and by Wilm and Kjer [64], available at MATLAB Central [65]. For the parametric active contour model, we modified code written by Kroon [66]. All other methods were implemented using original code.

2.4. Remeshing

Our registration method works best with prostate models containing triangulated meshes in which the vertices are as uniformly spaced as possible (*i.e.*, the lengths of all edges are approximately equal). It results in a more reliable orientation estimation for the affine registration, because each part of the surface is approximately equally represented in the PCA and ICP algorithms, and the active contour algorithm used for elastic surface registration showed more stable behavior with respect to self-intersection.

To obtain uniform meshes, a remesh algorithm using the non-adaptive part of the method described in [67] was applied to each of the surface models obtained from both histology and TRUS. This iterative method uses front propagation to find the location on the surface with the longest geodesic distance to all vertices that are already in the mesh; a new vertex is then inserted at that location. In this way, vertices are equally distributed over the surface, which leads to an uniform mesh. The number of vertices N in the mesh is a trade-off between computational speed and accurate representation of the prostate shape (hence higher registration accuracy for irregular surfaces). For our surface models we used $N = 2000$, which was sufficient to reproduce the encountered prostate deformations.

2.5. In vitro *validation*

Because natural landmarks are not always present in both histology and TRUS, an *in vitro* experiment, using phantoms with fiducial markers, was designed to quantitatively assess the registration error of the presented methods. Two gelatin phantoms of the prostate were produced and embedded in a gelatin surrounding (Figs. 4 and 5), based on the design presented in [68]. Different from [68], we chose to use gelatin as phantom material, because it suited the scope of our experiments and was easier to handle. The gelatin was constructed such that the prostate phantom was approximately three times stiffer than the surrounding gel.

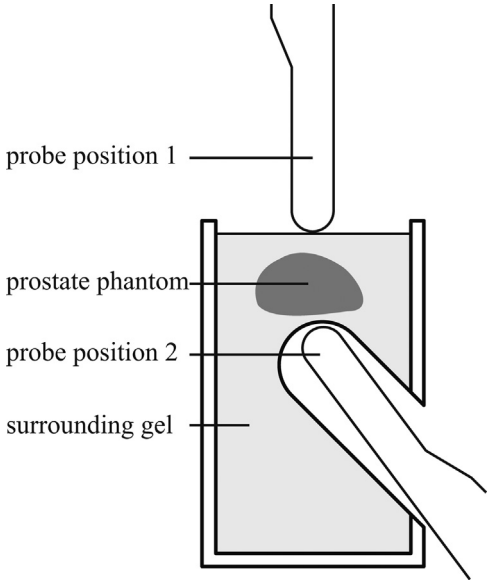

Fig. 4. Schematic side-view of the phantom used for *in vitro* validation.

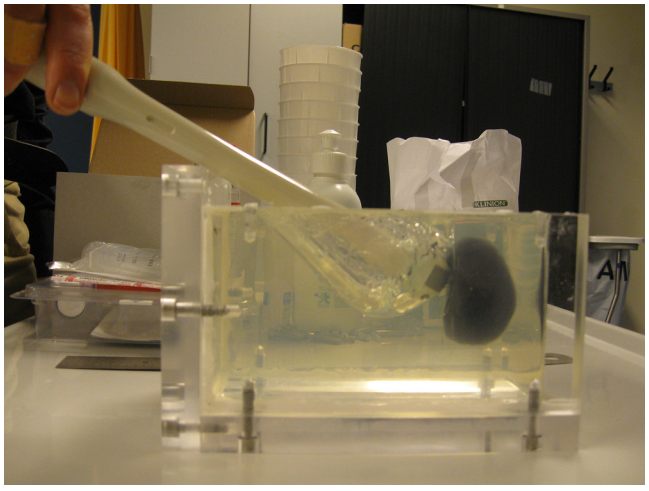

Fig. 5. A gelatin phantom while scanning in position 2.

To be able to distinguish the prostate phantom from the surrounding gel in TRUS B-mode images, a small amount of graphite powder was added to the prostate phantom as a scattering agent. Furthermore, in each phantom, 9 clay markers with a diameter of 3–5 mm were added for assessment of the TRE. A hole on the side (50 mm in diameter), large enough to accommodate and rotate a TRUS end-fire probe, represented the rectum, enabling simulation of TRUS imaging during a prostate examination (position 2). Alternatively, the prostate could be scanned from the top (position 1) to obtain images at a different angle than in position 1 and without phantom deformation due to pressure by the probe head, and therefore providing images that could represent the histology.

In this experiment, we used an iU22 (Philips Healthcare, Bothell, WA) US scanner with a 3D endocavity probe (3D9-3v) to exclude model construction from this validation. Each phantom was first scanned from position 1 to acquire an image of a "histology" phantom. Subsequently, each phantom was scanned with the same probe from position 2, while pushing the probe against the phantom to acquire a "TRUS" image. The latter scan was repeated 6 times with varying strength and location of the force applied on the phantom to test the robustness of the registration algorithm against varying deformations.

In each 3D US image, the phantom's contour and markers were manually segmented to construct 2000-node surface meshes with markers inside. For each phantom, all "TRUS" meshes (reference) were registered with the "histology" mesh (source) using the proposed algorithms. The TRE was defined to be the distance between a marker in the reference mesh to the same marker in the registered mesh. Results were stored after affine and elastic registration to evaluate the performance of the individual steps. The registration accuracy and execution time were compared for the different methods described in Section 2.3. The statistical significance (p-value) of the results was evaluated by two-sided Wilcoxon signed rank tests for paired data and by two-sided Wilcoxon rank sum tests for unpaired data.

The described *in vitro* experiment focused on validation of the registration algorithm only, leaving out the construction of the model from 2D images and deformations due to surgery and the fixation process.

2.6. In vivo *validation*

In 7 patients, (parts of) the border between the peripheral and central zone (BPZ) of the prostate (see Fig. 1) was visible both in the histology and TRUS images. These patients were therefore selected for *in vivo* validation using the BPZs as landmarks to evaluate the TRE. In two patients, two ultrasound recordings were made at different dates and were both included. As a result, a total of 9 prostate model sets were used for validation. Different from the *in vitro* experiments, the *in vivo* validation included model construction and the effect of deformation after surgery.

The BPZ was manually drawn in the TRUS and histology images by an expert, after which 3D models were reconstructed as described in Section 2.2. Between the images, the BPZ was interpolated using a linear radial basis function with noise reduction [69,70]. The constructed models were then registered. The TRE was determined by calculating the normals to the surface of the registered (histology) BPZ and finding the point at which it intersected with the reference (TRUS) surface. The distance between the histology and TRUS surfaces along a surface normal was defined to be the TRE at that point. However, because TRUS and histology showed also BPZ parts that were not corresponding, the corresponding parts had to be defined for the validation. Parts of the BPZ for which no intersection point was found along the surface normal were considered to be non-corresponding, and were therefore ignored. Statistical analysis of the results was done in a similar way as described in Section 2.5.

Because the models were constructed by stacking contours from base to apex, as described in Section 2.2, the patient models already had a similar orientation. For this reason, the TRE was also determined for registration without applying rotation in the stepwise affine transformation.

3. Results

3.1. In vitro *validation*

An example of the registered phantom models with markers after affine and elastic registration is shown in Fig. 6. The model shapes showed already good agreement after affine registration, but a slight mismatch could be observed due to deformation by the imaging probe. After elastic registration, the two models almost completely overlapped, as expected.

In Table 2, the TREs are summarized for each registration method. For each measurement, the means and standard deviations were computed over all markers (9 per phantom). Then, the means and standard deviations were computed over all

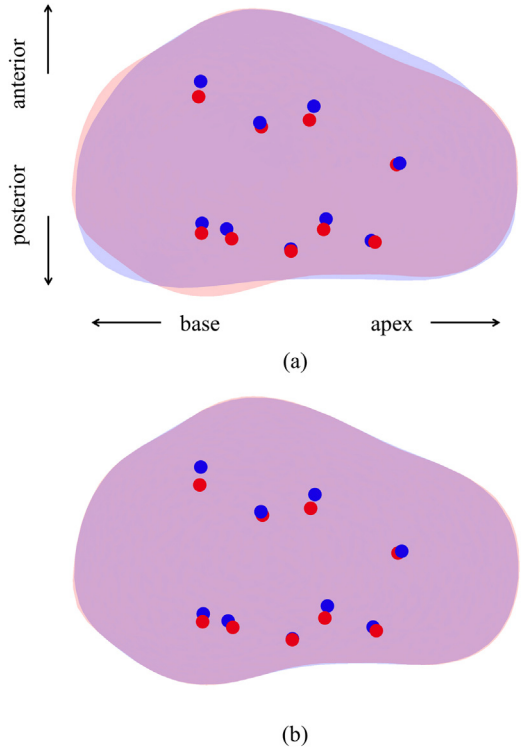

Fig. 6. Registration of phantom models (containing 9 landmarks) imaged in position 1 (blue) and in position 2 (red). (a) Affine registration by the ICP algorithm using a rigid transformation with anisotropic scaling. (b) The same affine registration followed by elastic registration using NN interpolation. (For interpretation of the references to color in this figure legend, the reader is referred to the web version of the article.)

measurements (6 per phantom). Rotation by PCA resulted in an average TRE of over 8 mm for phantom 1, but below 2 mm for phantom 2. The reason for this difference resides in the observation that, different from phantom 2, no clear second main axis perpendicular to the first main axis could be distinguished for phantom 1. The ICP method performed well in both phantoms. No significant difference was observed with respect to the mean TRE after applying elastic registration ($p \in [0.93, 0.97]$) using FE interpolation, and for NN interpolation the mean TRE was even significantly higher ($p < 0.001$) for each ICP method.

The computation time for any of the affine registration methods was negligible compared to the computation time of the elastic registration techniques. Also, the type of scaling used in the affine registration step had little influence on the computation time required for the elastic registration. Using NN instead of FE for internal registration reduced the computation time by approximately a factor 10.

3.2. In vivo *validation*

Table 3 gives the TREs per method based on 9 TRUS-histology registrations in 7 patients (see Section 2.6). The results for the methods without scaling are omitted, because in some cases the shape differences between the reference and source model were too large after rigid registration only. In those cases, parts of the source model were not covered by the blurred reference image in the elastic surface registration. In those uncovered parts, elastic registration did not work and, consequently, the internal deformations could not be computed.

The mean TRE was lower for the ICP methods than for the PCA methods. This difference was significant for the transformation including IS ($p < 0.027$), but not significant for AS ($p = 0.074$). Applying elastic registration using NN interpolation after affine registration decreased the TRE significantly for rigid ICP + IS and rigid ICP + AS ($p < 0.01$) and insignificantly for the other methods ($p \in [0.055, 0.20]$). Interpolation by FE even increased the TRE,

Table 2
Results of the *in vitro* validation: mean ± standard deviation – computed over all measurements – of computation time, mean TRE, and standard deviation (in brackets) of the TRE computed over 9 markers per measurement.

Method	Computation time (s)	TRE phantom 1 (mm)	TRE phantom 2 (mm)	TRE overall (mm)
PCA	0.0 ± 0.0	8.0 ± 2.5 (1.8 ± 0.5)	1.4 ± 0.4 (0.5 ± 0.2)	4.7 ± 3.9 (1.1 ± 0.8)
PCA + NN	17.4 ± 1.0	8.3 ± 2.7 (1.6 ± 0.4)	1.5 ± 0.4 (0.5 ± 0.2)	4.9 ± 4.0 (1.1 ± 0.7)
PCA + FE	175.9 ± 4.7	8.6 ± 3.0 (1.3 ± 0.2)	1.6 ± 0.5 (0.5 ± 0.1)	5.1 ± 4.2 (0.9 ± 0.5)
PCA + IS	0.3 ± 0.0	8.0 ± 2.5 (1.8 ± 0.5)	1.4 ± 0.4 (0.5 ± 0.2)	4.7 ± 3.9 (1.1 ± 0.8)
PCA + IS + NN	17.1 ± 1.2	8.3 ± 2.7 (1.6 ± 0.4)	1.5 ± 0.4 (0.5 ± 0.2)	4.9 ± 4.0 (1.1 ± 0.7)
PCA + IS + FE	170.1 ± 5.6	8.6 ± 3.0 (1.3 ± 0.2)	1.6 ± 0.5 (0.5 ± 0.1)	5.1 ± 4.2 (0.9 ± 0.5)
PCA + AS	0.0 ± 0.0	8.1 ± 2.6 (1.7 ± 0.5)	1.4 ± 0.4 (0.5 ± 0.1)	4.8 ± 3.9 (1.1 ± 0.7)
PCA + AS + NN	16.9 ± 0.7	8.4 ± 3.0 (1.6 ± 0.4)	1.4 ± 0.4 (0.4 ± 0.2)	4.9 ± 4.1 (1.0 ± 0.7)
PCA + AS + FE	167.9 ± 0.7	8.6 ± 3.0 (1.3 ± 0.2)	1.5 ± 0.4 (0.5 ± 0.1)	5.1 ± 4.2 (0.9 ± 0.5)
ICP rigid	0.5 ± 0.3	1.7 ± 0.2 (0.8 ± 0.3)	1.3 ± 0.1 (0.5 ± 0.1)	1.5 ± 0.3 (0.7 ± 0.3)
ICP rigid + NN	17.2 ± 0.9	1.8 ± 0.2 (0.9 ± 0.3)	1.3 ± 0.1 (0.5 ± 0.1)	1.6 ± 0.3 (0.7 ± 0.3)
ICP rigid + FE	168.7 ± 6.2	1.7 ± 0.2 (1.1 ± 0.3)	1.3 ± 0.1 (0.4 ± 0.1)	1.5 ± 0.2 (0.8 ± 0.4)
ICP rigid + IS	0.4 ± 0.0	1.7 ± 0.3 (0.8 ± 0.3)	1.2 ± 0.1 (0.5 ± 0.1)	1.5 ± 0.3 (0.7 ± 0.3)
ICP rigid + IS + NN	17.1 ± 0.6	1.9 ± 0.3 (0.9 ± 0.3)	1.3 ± 0.1 (0.5 ± 0.1)	1.6 ± 0.3 (0.7 ± 0.3)
ICP rigid + IS + FE	169.7 ± 5.4	1.7 ± 0.2 (1.1 ± 0.3)	1.3 ± 0.1 (0.4 ± 0.1)	1.5 ± 0.2 (0.7 ± 0.4)
ICP rigid + AS	0.7 ± 0.1	1.7 ± 0.2 (0.8 ± 0.2)	1.2 ± 0.1 (0.4 ± 0.1)	1.5 ± 0.3 (0.6 ± 0.3)
ICP rigid + AS + NN	16.9 ± 0.6	1.8 ± 0.2 (0.9 ± 0.2)	1.3 ± 0.1 (0.4 ± 0.1)	1.5 ± 0.3 (0.7 ± 0.3)
ICP rigid + AS + FE	169.6 ± 4.7	1.7 ± 0.2 (1.1 ± 0.2)	1.2 ± 0.1 (0.5 ± 0.1)	1.5 ± 0.3 (0.8 ± 0.4)
IS	0.3 ± 0.0	3.5 ± 0.6 (1.2 ± 0.1)	3.2 ± 0.4 (1.3 ± 0.3)	3.4 ± 0.5 (1.2 ± 0.2)
IS + NN	16.8 ± 0.5	3.3 ± 0.5 (1.3 ± 0.2)	3.2 ± 0.4 (1.1 ± 0.3)	3.2 ± 0.5 (1.2 ± 0.2)
IS + FE	171.8 ± 3.0	3.5 ± 0.5 (1.5 ± 0.2)	3.6 ± 0.4 (1.1 ± 0.3)	3.5 ± 0.4 (1.3 ± 0.3)
AS	0.0 ± 0.0	3.6 ± 0.6 (1.3 ± 0.1)	3.2 ± 0.4 (1.2 ± 0.3)	3.4 ± 0.5 (1.3 ± 0.2)
AS + NN	16.5 ± 0.7	3.3 ± 0.6 (1.4 ± 0.2)	3.1 ± 0.4 (1.1 ± 0.3)	3.2 ± 0.5 (1.2 ± 0.3)
AS + FE	170.8 ± 4.0	3.6 ± 0.5 (1.3 ± 0.1)	3.7 ± 0.4 (1.1 ± 0.3)	3.6 ± 0.4 (1.3 ± 0.4)

PCA = principal component analysis, ICP = iterative closest point, IS = isotropic scaling, AS = anisotropic scaling, NN = natural neighbor, FE = finite element.

Table 3
Results of the *in vivo* validation: mean ± standard deviation – computed over all measurements – of computation time, mean TRE, and standard deviation (in brackets) of the TRE computed within a measurement.

Method	Computation time (s)	TRE (mm)
PCA + IS	0.2 ± 0.0	3.0 ± 0.6 (2.0 ± 0.8)
PCA + IS + NN	37.9 ± 7.7	2.7 ± 1.0 (1.9 ± 1.3)
PCA + IS + FE	160.0 ± 8.4	3.6 ± 1.7 (2.8 ± 1.6)
PCA + AS	0.0 ± 0.0	2.9 ± 0.7 (2.0 ± 0.9)
PCA + AS + NN	37.2 ± 7.2	2.5 ± 0.9 (1.8 ± 1.1)
PCA + AS + FE	162.7 ± 10.5	3.6 ± 1.7 (3.0 ± 1.9)
ICP rigid + IS	0.3 ± 0.1	2.4 ± 0.5 (1.6 ± 0.5)
ICP rigid + IS + NN	37.6 ± 8.4	2.2 ± 0.6 (1.5 ± 0.5)
ICP rigid + IS + FE	161.4 ± 12.7	2.9 ± 0.9 (2.3 ± 0.8)
ICP rigid + AS	0.4 ± 0.1	2.4 ± 0.7 (1.6 ± 0.7)
ICP rigid + AS + NN	35.8 ± 7.7	2.2 ± 0.6 (1.6 ± 0.6)
ICP rigid + AS + FE	162.3 ± 7.3	2.7 ± 0.7 (2.0 ± 0.7)
IS	0.3 ± 0.0	2.6 ± 0.6 (1.6 ± 0.5)
IS + NN	43.5 ± 6.1	2.2 ± 0.5 (1.4 ± 0.4)
IS + FE	174.2 ± 18.2	2.9 ± 1.3 (2.2 ± 1.0)
AS	0.0 ± 0.0	2.5 ± 0.5 (1.6 ± 0.5)
AS + NN	42.0 ± 6.8	2.1 ± 0.5 (1.4 ± 0.3)
AS + FE	175.9 ± 18.5	2.8 ± 1.2 (2.4 ± 1.0)

although not significantly ($p \in [0.13, 0.65]$). When applying only scaling without automatic rotation in the affine step, the performance of the stepwise registration was similar to the performance of the methods using ICP as an affine registration step. The computation time for the NN interpolation was longer than in Table 2 ($p < 0.001$), because the BPZ contained more points to register than the 9 fiducial markers used in the phantom experiments. An example of a registration of two models using one of the best performing methods (ICP rigid + AS followed by NN) is given in Fig. 7.

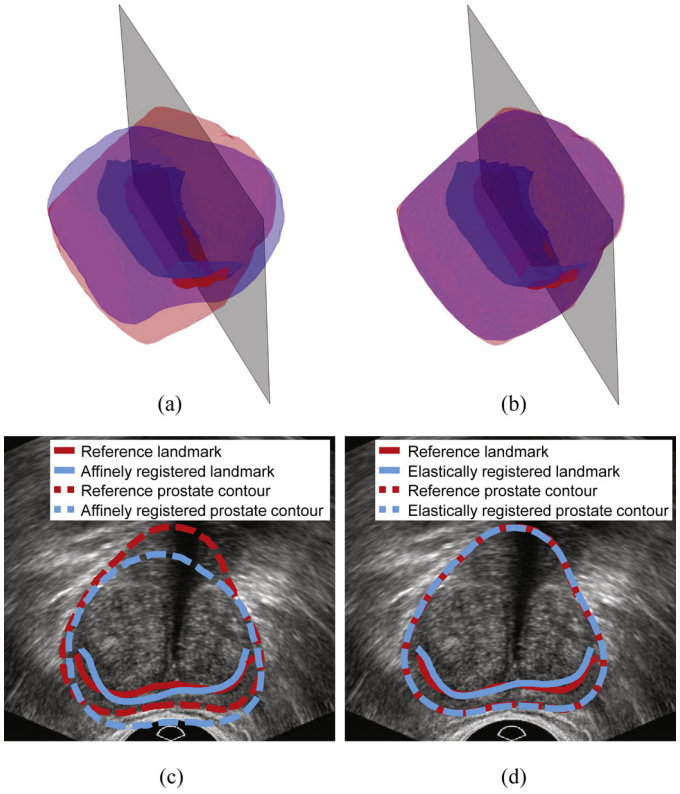

Fig. 7. Registration in one patient included in the validation. Red represents TRUS, blue represents histology. Subfigure (a) shows the result of the affine registration using the ICP algorithm with anisotropic scaling. Subfigure (b) shows the elastic registration using NN interpolation, after applying the same affine registration as in (a). In (c) and (d), cross-cuts are shown at the planes indicated in (a) and (b), respectively. (For interpretation of the references to color in this figure legend, the reader is referred to the web version of the article.)

4. Discussion

The phantom experiments resulted in a mean TRE of 1.5 mm for the best performing method; *in vivo*, this value was 2.1 mm. This error is acceptable for most clinical purposes, since tumors are considered clinically significant when their volumes exceed 0.5 cm^3 [71]. Assuming a spherical shape, this yields a tumor diameter of 10 mm. TREs were comparable with the results presented in the literature [38,39], in which surface-based registration was applied to prostates imaged in different modalities. However, in [38,39], registration was not performed between *in vivo* and *ex vivo* images, bypassing the deformation due to surgery.

In the phantom experiments, TREs due to model construction or to deformation caused by surgery and preparation of the prostate for histopathologic analysis were not included. Although these differences were included in the *in vivo* study, the TREs in that study were only approximately 1 mm larger than those in the *in vitro* study. This suggests that the error introduced by our method used for model construction is relatively small.

From the lower standard deviations in the TREs in both the *in vitro* (Table 2) and the *in vivo* experiments (Table 3), it can be concluded that the ICP method is more robust in affine registration than the PCA-based method. The reason can possibly be found in the fact that the PCA method tries to find three main axes like those in an ellipsoid. Because the shape of the prostate in TRUS can be deformed drastically at the posterior side by the pressure of the probe head on the prostate, it does not resemble an ellipsoid-like shape anymore. In this case, the three orthogonal main axes to estimate the orientation of the prostate model cannot be correctly defined.

Surprisingly, *in vivo*, registration without applying automatic rotation performed similar to the ICP methods. Because both models were constructed by stacking slices from base to apex, they had already been reasonably well-aligned before applying the registration algorithm. The same *a priori* information could be applied in the validation of some PCa techniques using other imaging modalities, such as MRI, where histology slices and imaging planes are already well aligned before registration.

When comparing *in vitro* average TREs (Table 2) for affine ICP and elastic registration, only small differences were observed (<0.1 mm). An explanation for this result could be that most of the deformation could already be covered by the affine registration. Errors in drawing the contours of the phantoms and markers were probably larger than the improvement that could be made by elastic registration. In our *in vivo* experiments, the elastic registration followed by NN interpolation did result in a small decrease in TRE for each affine registration method. The FE method, however, resulted in higher TREs. The deformation at the surface defined by the elastic surface registration of the affinely registered models probably did not represent realistic boundary conditions for a physics-based model. A more general interpolation method, such as the NN interpolation, could then result in lower TRE.

Although the differences between the TREs for affine and elastic registration were small, the differences could be larger close to the surface. An example of the registration of histopathology and TRUS using an affine and an elastic method is given in Fig. 8. In this case, the deformation at the posterior surfaces – caused by probe pressure – could not be compensated for by an affine transformation. As a result, part of the registered tumor lied outside the prostate and could therefore not be used for validation or training

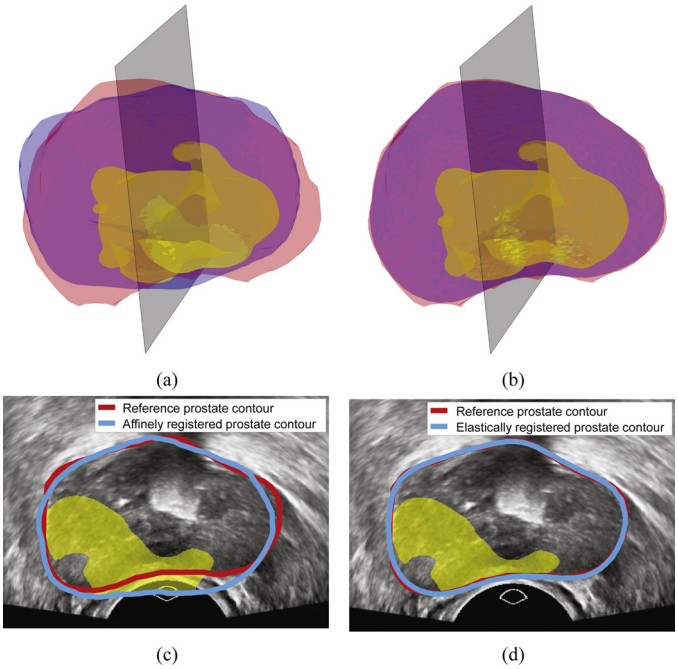

Fig. 8. Registration of 2 prostate models containing a tumor (yellow). Red represents TRUS, blue represents histology. Subfigure (a) shows the result of the affine registration using the ICP algorithm with anisotropic scaling. Subfigure (b) shows the elastic registration using NN interpolation, after applying the same affine registration as in (a). In (c) and (d), cross-cuts are shown at the planes indicated in (a) and (b), respectively. (For interpretation of the references to color in this figure legend, the reader is referred to the web version of the article.)

of a PCa imaging technique. Applying an elastic registration using NN interpolation solved this issue.

Because the location of the BPZ in between histology slices was unknown and had to be interpolated, an inaccuracy in the estimation of the TRE in the *in vivo* validation was possibly introduced. Moreover, the orientation of the BPZ is largely parallel to the apex-base axis. Because the TREs were estimated based on the surface normals of the BPZ, the influence of registration errors in that direction on the final TRE was smaller than in other directions. Fiducial point landmarks could provide a more accurate reference for TRE estimation, but can be difficult to apply during a regular TRUS examination.

Although outside the scope of this work, a method was given to construct 3D prostate models from a transversal sweep video. The presented method requires manual delineation of the prostate contours to obtain the most accurate models and registration. However, an accurate (semi-)automatic segmentation could assist in making this step less time-consuming. Moreover, the accuracy of the model construction could benefit from using a 3D US probe to minimize the error made by the conversion from 2D sweep video to 3D US.

The presented method does not rely on the mechanical properties of the prostate and, therefore, assumes a homogeneous material. The prostate, however, consists of different zones with different stiffness [40]. Moreover, tumors are known to be stiffer than healthy prostate tissue [40]. When the location of the central zone and the tumors are known, it could be worth applying varying stiffness settings in the internal registration step to reduce the TRE.

5. Conclusions

Several methods, directly applicable in clinical practice, for 3D, affine and elastic, surface-based registration of prostate models obtained by TRUS imaging and histology were compared both *in vitro* and *in vivo*. Experiments using two gelatin phantoms with fiducial markers resulted in a mean TRE of 1.5 ± 0.2 mm for the best performing method. The mean TRE obtained from validation in 7 patients was 2.1 ± 0.5 mm, which is below the slicing thickness in histology or the size of clinically significant tumors. The ICP algorithm proved to be a robust approach for affine registration, whereas rotation using a PCA approach frequently resulted in large TREs. For the elastic registration, the NN interpolation outperformed a FE approach assuming linearly elastic material. Because the algorithm used for registration is independent of the adopted imaging technique, applications for imaging modalities other than TRUS (such as MR) can be envisaged.

Conflict of interest statement

The authors declare that they have no conflicts of interest.

Acknowledgement

This work was supported by the European Research Council under Starting Grant #280209.

References

[1] Siegel RL, Miller KD, Jemal A. Cancer statistics, 2015. CA Cancer J Clin 2015;65(1):5–29, http://dx.doi.org/10.3322/caac.21254.
[2] Zaytoun OM, Anil T, Moussa AS, Jianbo L, Fareed K, Jones JS. Morbidity of prostate biopsy after simplified versus complex preparation protocols: assessment of risk factors. Urology 2011;77(4):910–4, http://dx.doi.org/10.1016/j.urology.2010.12.033.
[3] Singh H, Canto EI, Shariat SF, Kadmon D, Miles BJ, Wheeler TM, et al. Predictors of prostate cancer after initial negative systematic 12 core biopsy. J Urol 2004;171(5):1850–4, http://dx.doi.org/10.1097/01.ju.0000119667.86071.e7.
[4] Kvåle R, Møller B, Wahlqvist R, Fosså SD, Berner A, Busch C, et al. Concordance between Gleason scores of needle biopsies and radical prostatectomy specimens: a population-based study. BJU Int 2009;103(12):1647–54, http://dx.doi.org/10.1111/j.1464-410X.2008.08255.x.
[5] Bangma C, Roemeling S, Schröder F. Overdiagnosis and overtreatment of early detected prostate cancer. World J Urol 2007;25:3–9, http://dx.doi.org/10.1007/s00345-007-0145-z.
[6] Klotz L. Prostate cancer overdiagnosis and overtreatment. Curr Opin Endocrinol Diabetes Obes 2013;20(3):204–9, http://dx.doi.org/10.1097/MED.0b013e328360332a.
[7] Ukimura O, de Castro Abreu AL, Gill IS, Shoji S, Hung AJ, Bahn D. Image visibility of cancer to enhance targeting precision and spatial mapping biopsy for focal therapy of prostate cancer. BJU Int 2013;111(8):E354–64, http://dx.doi.org/10.1111/bju.12124.
[8] Sommer G, Bouley D, Gill H, Daniel B, Pauly Butts K, Diederich C. Focal ablation of prostate cancer: four roles for magnetic resonance imaging guidance. Can J Urol 2013;20(2):6672–81.
[9] Alonzi R, Padhani AR, Allen C. Dynamic contrast enhanced MRI in prostate cancer. Eur J Radiol 2007;63(3):335–50, http://dx.doi.org/10.1016/j.ejrad.2007.06.028.
[10] Hegde JV, Mulkern RV, Panych LP, Fennessy FM, Fedorov A, Maier SE, et al. Multiparametric MRI of prostate cancer: an update on state-of-the-art techniques and their performance in detecting and localizing prostate cancer. J Magn Reson Imaging 2013;37(5):1035–54, http://dx.doi.org/10.1002/jmri.23860.
[11] Mischi M, Turco S, Lavini C, Kompatsiari K, de la Rosette JJMCH, Breeuwer M, et al. Magnetic resonance dispersion imaging for localization of angiogenesis and cancer growth. Invest Radiol 2014;49(8):561–9, http://dx.doi.org/10.1097/RLI.0000000000000056.
[12] Moradi M, Mousavi P, Abolmaesumi P. Computer-aided diagnosis of prostate cancer with emphasis on ultrasound-based approaches: a review. Ultrasound Med Biol 2007;33(7):1010–28, http://dx.doi.org/10.1016/j.ultrasmedbio.2007.01.008.
[13] Grabski B, Baeurle L, Loch A, Wefer B, Paul U, Loch T. Computerized transrectal ultrasound of the prostate in a multicenter setup (C-TRUS-MS): detection of cancer after multiple negative systematic random and in primary biopsies. World J Urol 2011;29(5):573–9, http://dx.doi.org/10.1007/s00345-011-0713-0.
[14] Barr RG, Memo R, Schaub CR. Shear wave ultrasound elastography of the prostate: initial results. Ultrasound Q 2012;28(1):13–20, http://dx.doi.org/10.1097/RUQ.0b013e318249f594.
[15] Ahmad S, Cao R, Varghese T, Bidaut L, Nabi G. Transrectal quantitative shear wave elastography in the detection and characterisation

of prostate cancer. Surg Endosc 2013;27(9):3280–7, http://dx.doi.org/10.1007/s00464-013-2906-7.
[16] Correas JM, Tissier AM, Khairoune A, Khoury G, Eiss D, Hélénon O. Ultrasound elastography of the prostate: state of the art. Diagn Interv Imaging 2013;94(5):551–60, http://dx.doi.org/10.1016/j.diii.2013.01.017.
[17] Boehm K, Salomon G, Beyer B, Schiffmann J, Simonis K, Graefen M, et al. Shear wave elastography for localization of prostate cancer lesions and assessment of elasticity thresholds: implications for targeted biopsies and active surveillance protocols. J Urol 2015;193(3):794–800, http://dx.doi.org/10.1016/j.juro.2014.09.100.
[18] Postema AW, Frinking PJ, Smeenge M, De Reijke TM, De la Rosette JJ, Tranquart F, et al. Dynamic contrast-enhanced ultrasound parametric imaging for the detection of prostate cancer. BJU Int 2015, http://dx.doi.org/10.1111/bju.13116 [in press].
[19] Schalk S, Demi L, Smeenge M, Mills D, Wallace K, de la Rosette J, et al. 4-d spatiotemporal analysis of ultrasound contrast agent dispersion for prostate cancer localization: a feasibility study. IEEE Trans Ultrason Ferroelectr Freq Control 2015;62(5):839–51, http://dx.doi.org/10.1109/TUFFC.2014.006907.
[20] Kuenen M, Saidov T, Wijkstra H, de La Rosette J, Mischi M. Correspondence – spatiotemporal correlation of ultrasound contrast agent dilution curves for angiogenesis localization by dispersion imaging. IEEE Trans Ultrason Ferroelectr Freq Control 2013;60(12):2665–9, http://dx.doi.org/10.1109/TUFFC.2013.2865.
[21] Trivedi H, Turkbey B, Rastinehad AR, Benjamin CJ, Bernardo M, Pohida T, et al. Use of patient-specific MRI-based prostate mold for validation of multiparametric MRI in localization of prostate cancer. Urology 2012;79(1):233–9, http://dx.doi.org/10.1016/j.urology.2011.10.002.
[22] Zalesky M, Urban M, Smerhovsk Z, Zachoval R, Lukes M, Heracek J. Value of power Doppler sonography with 3D reconstruction in preoperative diagnostics of extraprostatic tumor extension in clinically localized prostate cancer. Int J Urol 2008;15(1):68–75, http://dx.doi.org/10.1111/j. 1442-2042.2007.01926.x.
[23] Braeckman J, Autier P, Soviany C, Nir R, Nir D, Michielsen D, et al. The accuracy of transrectal ultrasonography supplemented with computer-aided ultrasonography for detecting small prostate cancers. BJU Int 2008;102(11):1560–5, http://dx.doi.org/10.1111/j.1464-410X.2008.07878.x.
[24] Engelbrecht MR, Huisman HJ, Laheij RJF, Jager GJ, van Leenders GJLH, Hulsbergen-Van De Kaa CA, et al. Discrimination of prostate cancer from normal peripheral zone and central gland tissue by using dynamic contrast-enhanced MR imaging. Radiology 2003;229(1):248–54, http://dx.doi.org/10.1148/radiol.2291020200.
[25] Mottet N, Bellmunt J, Briers E, van den Bergh R, Bolla M, van Casteren N, et al. Guidelines on prostate cancer – update March 2015. European Association of Urology; 2015. Available from: http://uroweb.org/guideline/prostate-cancer/ [cited 19.03.15].
[26] Mazaheri Y, Bokacheva L, Kroon DJ, Akin O, Hricak H, Chamudot D, et al. Semi-automatic deformable registration of prostate MR images to pathological slices. J Magn Reson Imaging 2010;32(5):1149–57, http://dx.doi.org/10.1002/jmri.22347.
[27] Chappelow J, Bloch BN, Rofsky N, Genega E, Lenkinski R, DeWolf W, et al. Elastic registration of multimodal prostate MRI and histology via multiattribute combined mutual information. Med Phys 2011;38(4):2005–18, http://dx.doi.org/10.1118/1.3560879.
[28] Xiao G, Bloch BN, Chappelow J, Genega EM, Rofsky NM, Lenkinski RE, et al. Determining histology-MRI slice correspondences for defining MRI-based disease signatures of prostate cancer. Comput Med Imaging Graph 2011;35(78):568–78, http://dx.doi.org/10.1016/j.compmedimag.2010.12.003.
[29] Groenendaal G, Moman MR, Korporaal JG, van Diest PJ, van Vulpen M, Philippens ME, et al. Validation of functional imaging with pathology for tumor delineation in the prostate. Radiother Oncol 2010;94(2):145–50, http://dx.doi.org/10.1016/j.radonc.2009.12.034.
[30] Ward AD, Crukley C, McKenzie CA, Montreuil J, Gibson E, Romagnoli C, et al. Prostate: registration of digital histopathologic images to in vivo MR images acquired by using endorectal receive coil. Radiology 2012;263(3):856–64, http://dx.doi.org/10.1148/radiol.12102294.
[31] Shah V, Pohida T, Turkbey B, Mani H, Merino M, Pinto PA, et al. A method for correlating in vivo prostate magnetic resonance imaging and histopathology using individualized magnetic resonance-based molds. Rev Sci Instrum 2009;80(10):104301, http://dx.doi.org/10.1063/1.3242697.
[32] Priester A, Natarajan S, Le JD, Garritano J, Radosavcev B, Grundfest W, et al. A system for evaluating magnetic resonance imaging of prostate cancer using patient-specific 3D printed molds. Am J Clin Exp Urol 2014;2(2):127–35.
[33] Park H, Piert MR, Khan A, Shah R, Hussain H, Siddiqui J, et al. Registration methodology for histological sections and in vivo imaging of human prostate. Acad Radiol 2008;15(8):1027–39, http://dx.doi.org/10.1016/j.acra.2008.01.022.
[34] Taylor LS, Porter BC, Nadasdy G, di Sant'Agnese PA, Pasternack D, Wu Z, et al. Three-dimensional registration of prostate images from histology and ultrasound. Ultrasound Med Biol 2004;30(2):161–8, http://dx.doi.org/10.1016/j.ultrasmedbio.2003.10.005.
[35] Moskalik A, Carson P, Rubin J, Fowlkes J, Wojno K, Bree R. 3D registration of ultrasound with histology in the prostate. In: Proc. of IEEE Int. Ultrason. Symp., vol. 2. 1997. p. 1397–400, http://dx.doi.org/10.1109/ULTSYM.1997.661838.
[36] Nir G, Sahebjavaher R, Kozlowski P, Chang S, Jones E, Goldenberg S, et al. Registration of whole-mount histology and volumetric imaging of the prostate using particle filtering. IEEE Trans Med Imaging 2014;33(8):1601–13, http://dx.doi.org/10.1109/TMI.2014.2319231.
[37] Schned AR, Wheeler KJ, Hodorowski CA, Heaney JA, Ernstoff MS, Amdur RJ, et al. Tissue-shrinkage correction factor in the calculation of prostate cancer volume. Am J Surg Pathol 1996;20(12):1501–6.
[38] Crouch J, Pizer S, Chaney E, Hu YC, Mageras G, Zaider M. Automated finite-element analysis for deformable registration of prostate images. IEEE Trans Med Imaging 2007;26(10):1379–90, http://dx.doi.org/10.1109/TMI.2007.898810.
[39] Lee HP, Foskey M, Niethammer M, Krajcevski P, Lin MC. Simulation-based joint estimation of body deformation and elasticity parameters for medical image analysis. IEEE Trans Med Imaging 2012;31(11):2156–68, http://dx.doi.org/10.1109/TMI.2012.2212450.
[40] Zhai L, Madden J, Foo WC, Palmeri ML, Mouraviev V, Polascik TJ, et al. Acoustic radiation force impulse imaging of human prostates ex vivo. Ultrasound Med Biol 2010;36(4):576–88, http://dx.doi.org/10.1016/j.ultrasmedbio.2009.12.006.
[41] Hoyt K, Castaneda B, Zhang M, Nigwekar P, di Sant'Agnese PA, Joseph JV, et al. Tissue elasticity properties as biomarkers for prostate cancer. Cancer Biomark 2008;4(4):213–25.
[42] Zhang M, Nigwekar P, Castaneda B, Hoyt K, Joseph JV, di Sant'Agnese A, et al. Quantitative characterization of viscoelastic properties of human prostate correlated with histology. Ultrasound Med Biol 2008;34(7):1033–42, http://dx.doi.org/10.1016/j.ultrasmedbio.2007.11.024.
[43] Phipps S, Yang T, Habib F, Reuben R, McNeill S. Measurement of the mechanical characteristics of benign prostatic tissue: a novel method for assessing benign prostatic disease. Urology 2005;65(5):1024–8, http://dx.doi.org/10.1016/j.urology.2004.12.022.
[44] Krouskop TA, Wheeler TM, Kallel F, Garra BS, Hall T. Elastic moduli of breast and prostate tissues under compression. Ultrason Imaging 1998;20(4):260–74, http://dx.doi.org/10.1177/016173469802000403.
[45] Tutar IB, Dev Pathak S, Kim Y. 3D prostate shape modeling from sparsely-acquired 2D images using deformable models. In: Proc. SPIE, Medical Imaging; vol. 5376. 2004. p. 524–32, http://dx.doi.org/10.1117/12.536809.
[46] Cool D, Downey D, Izawa J, Chin J, Fenster A. 3D prostate model formation from non-parallel 2D ultrasound biopsy images. Med Image Anal 2006;10(6):875–87, http://dx.doi.org/10.1016/j.media.2006.09.001.
[47] Chen L, Ho H, Lazaro R, Thng C, Yuen J, Ng W, et al. Optimum slicing of radical prostatectomy specimens for correlation between histopathology and medical images. Int J Comput Assist Radiol Surg 2010;5(5):471–87, http://dx.doi.org/10.1007/s11548-010-0405-z.
[48] Gibson E, Gaed M, Gmez JA, Moussa M, Romagnoli C, Pautler S, et al. 3D prostate histology reconstruction: an evaluation of image-based and fiducial-based algorithms. Med Phys 2013;40(9):093501, http://dx.doi.org/10.1118/1.4816946.
[49] Besl P, McKay ND. A method for registration of 3-D shapes. IEEE Trans Pattern Anal Mach Intell 1992;14(2):239–56, http://dx.doi.org/10.1109/34.121791.
[50] Arun K, Huang T, Blostein S. Least-squares fitting of two 3-D point sets. IEEE Trans Pattern Anal Mach Intell 1987;PAMI-9(5):698–700, http://dx.doi.org/10.1109/TPAMI.1987.4767965.
[51] Levenberg K. A method for the solution of certain problems in least-squares. Q Appl Math 1944;2:164–8.
[52] Marquardt DW. An algorithm for least-squares estimation of nonlinear parameters. J Soc Ind Appl Math 1963;11(2):431–41, http://dx.doi.org/10.1137/0111030.
[53] Yi W, Marshall S. Principal component analysis in application to object orientation. Geo Spat Inf Sci 2000;3(3):76–8, http://dx.doi.org/10.1007/BF02826615.
[54] Kass M, Witkin A, Terzopoulos D. Snakes: active contour models. Int J Comput Vis 1988;1(4):321–31, http://dx.doi.org/10.1007/BF00133570.
[55] Cohen LD. On active contour models and balloons. Comput Vis Graph Image Process 1991;53(2):211–8, http://dx.doi.org/10.1016/1049-9660(91)90028-N.
[56] Lürig C, Kobbelt L, Ertl T. Hierarchical solutions for the deformable surface problem in visualization. Graph Models 2000;62:2–18, http://dx.doi.org/10.1006/gmod.1999.0515.
[57] Ray N, Acton S, Altes T, de Lange E, Brookeman J. Merging parametric active contours within homogeneous image regions for MRI-based lung segmentation. IEEE Trans Med Imaging 2003;22(2):189–99, http://dx.doi.org/10.1109/TMI.2002.808354.
[58] Zimmer C, Labruyere E, Meas-Yedid V, Guillen N, Olivo-Marin JC. Segmentation and tracking of migrating cells in videomicroscopy with parametric active contours: a tool for cell-based drug testing. IEEE Trans Med Imaging 2002;21(10):1212–21, http://dx.doi.org/10.1109/TMI.2002.806292.
[59] Schwenninger D, Guttmann J, Moller K. Fast parametric active contour to improve 3D segmentation of tubular structures. In: Proc. of Int. Conf. Bioinform. Biomed. Eng. 2009. p. 1–4, http://dx.doi.org/10.1109/ICBBE.2009.5162849.
[60] Hensel JM, Mnard C, Chung PW, Milosevic MF, Kirilova A, Moseley JL, et al. Development of multiorgan finite element-based prostate deformation model enabling registration of endorectal coil magnetic resonance imaging for radiotherapy planning. Int J Radiat Oncol Biol Phys 2007;68(5):1522–8, http://dx.doi.org/10.1016/j.ijrobp.2007.04.004.

[61] Si H. TetGen, a Delaunay-based quality tetrahedral mesh generator. ACM Trans Math Softw 2015;41(2), http://dx.doi.org/10.1145/2629697, 11:1–11:36.
[62] Sibson R. A brief description of natural neighbor interpolation. In: Interpreting multivariate data. New York: John Wiley & Sons; 1981. p. 21–36.
[63] Kroon DJ. Finite iterative closest point; 2009. Available from: http://www.mathworks.com/matlabcentral/fileexchange/24301-finite-iterative-closest-point/ [downloaded January 2014].
[64] Wilm J, Kjer M. Iterative closest point; 2013. Available from: http://www.mathworks.com/matlabcentral/fileexchange/27804-iterative-closest-point/ [downloaded January 2014].
[65] The MathWorks. MATLAB Central. http://www.mathworks.nl/matlabcentral/.
[66] Kroon DJ. Snake: active contour; 2011. Available from: http://www.mathworks.com/matlabcentral/fileexchange/28149-snake—active-contour/ [downloaded January 2012].
[67] Peyré G, Cohen LD. Geodesic remeshing using front propagation. Int J Comput Vis 2006;69:145–56, http://dx.doi.org/10.1007/s11263-006-6859-3.
[68] Hungr N, Long JA, Beix V, Troccaz J. A realistic deformable prostate phantom for multimodal imaging and needle-insertion procedures. Med Phys 2012;39(4):2031–41, http://dx.doi.org/10.1118/1.3692179.
[69] Carr J, Fright W, Beatson R. Surface interpolation with radial basis functions for medical imaging. IEEE Trans Med Imaging 1997;16(1):96–107, http://dx.doi.org/10.1109/42.552059.
[70] Carr JC, Beatson RK, Cherrie JB, Mitchell TJ, Fright WR, McCallum BC, et al. Reconstruction and representation of 3D objects with radial basis functions. In: Proc. of SIGGRAPH. 2001. p. 67–76, http://dx.doi.org/10.1145/383259.383266.
[71] Epstein JI, Walsh PC, Carmichael M, Brendler C. Pathologic and clinical findings to predict tumor extent of nonpalpable (stage T1 c) prostate cancer. JAMA 1994;271(5):368–74, http://dx.doi.org/10.1001/jama.1994.03510290050036.